The RHESSI Imaging Concept

G. J. Hurford[1], E. J. Schmahl[2,3], R. A. Schwartz[3,4], A. J. Conway[5], M. J. Aschwanden[6], A. Csillaghy[7], B. R. Dennis[3], C. Johns-Krull[8], S. Krucker[1], R. P. Lin[1,9], J. McTiernan[1], T. R. Metcalf[6], J. Sato[10], D. M. Smith[1]

[1] *Space Sciences Laboratory, University of California, Berkeley, CA 94720*
[2] *Astronomy Department, University of Maryland, College Park, MD 20742*
[3] *Lab for Astronomy and Solar Physics, NASA Goddard Space Flight Center, Greenbelt, MD 20771*
[4] *NASA Goddard Space Flight Center / SSAI, Greenbelt, MD 20771*
[5] *Department of Physics and Astronomy, The Open University, Milton Keynes MK7 6AA, UK*
[6] *Lockheed Martin Advanced Technology Center, Solar & Astrophysics Laboratory, Dept. L9-41, Palo Alto, CA 94304*
[7] *University of Applied Sciences, CH-5210 Windisch, Switzerland*
[8] *Department of Physics and Astronomy, Rice University, Houston, TX 77005*
[9] *Department of Physics, University of California, Berkeley, CA 94720*
[10] *Department of Physics, Montana State University, Bozeman, MT 59717*

2002/08/08

Abstract.

The Reuven Ramaty High Energy Solar Spectroscopic Imager (*RHESSI*) observes solar hard X-rays and gamma-rays from 3 keV to 17 MeV with spatial resolution as high as 2.3 arcseconds. Instead of conventional optics, imaging is based on nine rotating modulation collimators that time-modulate the incident flux as the spacecraft rotates. Starting from the arrival time of individual photons, ground-based software then uses the modulated signals to reconstruct the image of the source.

The purpose of this paper is to convey both an intuitive feel and the mathematical basis for this imaging process. Following a review of the relevant hardware, the imaging principles and the basic back-projection method are described, along with their relation to Fourier transforms. Several specific algorithms (Clean, MEM, Pixons and Forward-Fitting) applicable to *RHESSI* imaging are briefly described. The characteristic strengths and weaknesses of this type of imaging are summarized.

Keywords: Sun : X-rays — Sun : Flares — Instruments — Image Processing — Numerical Methods

1. Introduction

The primary scientific objective of the Reuven Ramaty High Energy Solar Spectroscopic Imager (*RHESSI*) is the study of energy release and

particle acceleration in solar flares. This is accomplished by imaging-spectroscopy of solar hard X-rays and gamma-rays over a 3-keV to 17-MeV energy range with energy resolution of ∼1 keV, time resolution of ∼2 s or better, and spatial resolution as high as 2.3 arcseconds.

The only practical method of combining such angular resolution with high sensitivity in this energy range within the cost, mass and launch constraints of a small satellite is to use collimator-based Fourier-transform imaging. Coded-aperture imaging, often used in astrophysics, would not be practical in this situation, since it would require a hard X-ray detector with ∼20 micron spatial resolution to achieve this spatial resolution. (See Prince *et al.* (1988) for a review of imaging techniques.) One of the most powerful of the Fourier family of techniques is rotational modulation synthesis, first proposed by Mertz (1967) and implemented by Schnopper, Thompson and Watt (1968) for non-solar observations.

In a solar context, previous related instrumentation included the Hard X-ray Imaging Spectrometer (HXIS) (Van Beek *et al.*, 1980), a direct-imaging hard X-ray telescope flown on the Solar Maximum Mission. Although its multi-grid collimator (divided into $\sim 10^3$ subcollimators) achieved 8 arcsecond resolution, its one-to-one association of imaging pixels to detector elements seriously limited its sensitivity. A Rotating Modulation Collimator (RMC) was used for solar flare X-ray imaging with angular resolution of $28''$ in the 20-40 keV energy range on the Hinotori mission (Makashima *et al.*, 1977; Ohki *et al.*, 1982; Enome, 1982). Subsequently, the Hard X-ray Telescope (HXT) on the Yohkoh satellite used non-rotating Fourier synthesis with angular resolution of $\sim 8''$ in the 20-100 keV energy range (Kosugi *et al.*, 1991). A balloon-borne solar telescope with two RMCs, the High Energy Imaging Device (HEIDI) (Crannell *et al.*, 1994) was used as a vehicle for making several relevant engineering advances including the demonstration of a high-bandwidth, high-resolution solar aspect system and the development of error-analysis techniques for the RMC optical design.

Among the new features of *RHESSI* imaging are its high angular resolution, its use of aspect knowledge in place of precision pointing, its fine energy resolution and wide energy range viewed with a common set of grid 'optics', its relative immunity to alignment errors, its ability to self-calibrate its own instrumental response and its measurement of a large number ($\sim 10^3$) Fourier components for improved image quality.

An overview of the *RHESSI* mission is provided by Lin *et al.*, 2002. Further information can be found at the following web sites: http://ssl.berkeley.edu/hessi and http://hesperia.gsfc.nasa.gov/rhessidatacenter. The purpose of this paper is to describe the concepts and techniques

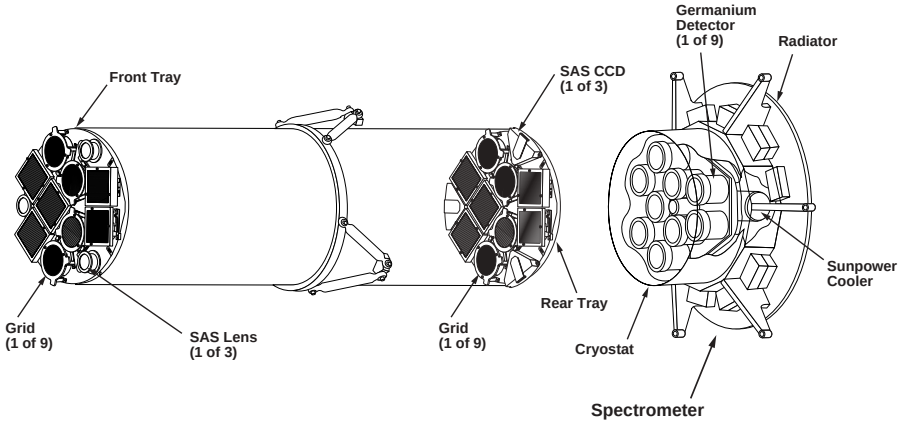

Figure 1. Perspective of the *RHESSI* imager. The key imager components are two identical sets of nine grids mounted on front and rear grid trays. A corresponding set of nine cooled germanium detectors is mounted behind the rear grids. The solar aspect system (SAS) consists of three lenses mounted on the front grid tray which focus optical images onto SAS CCDs on the rear grid tray.

of RMC imaging as implemented on *RHESSI*. An appreciation of the strengths and weaknesses of these techniques may prove useful both for making such images and for evaluating them.

2. The *RHESSI* Imager–A Brief Hardware Description

2.1. The Subcollimators

The *RHESSI* imaging hardware is described in detail by Zehnder *et al.* (2002). A schematic view (Figure 1) shows a set of nine bi-grid subcollimators, each consisting of a pair of widely separated grids in front of a corresponding non-imaging X-ray/gamma-ray detector. Each grid consists of a planar array of equally-spaced, X-ray-opaque slats separated by transparent slits. Within each subcollimator, the slits of the two grids are parallel and their pitches are identical. The nominal parameters of the *RHESSI* grids are listed in Table 1. Details of the grid geometry, calibration and response as a function of energy are given in a forthcoming paper by Hurford *et al.*

As illustrated in Figure 2, the transmission through the grid pair depends on the direction of the incident X-rays. If the direction of incidence is changed as a function of time, the transmission of the grid pair is modulated in time as the shadow of the slats in the top grid alternately falls on the slits or slats in the rear grid. For slits and slats

Table I. RHESSI – Nominal Grid Parameters

Subcollimator Number	1	2	3	4	5	6	7	8	9
Pitch (mm)	0.034	0.059	0.102	0.177	0.306	0.530	0.918	1.590	2.754
Slit Width (mm)	0.020	0.035	0.061	0.106	0.184	0.318	0.477	0.811	1.487
FWHM Resolution (arcsec)	2.26	3.92	6.79	11.76	20.36	35.27	61.08	105.8	183.2
Max. Transmission	0.60	0.60	0.60	0.60	0.60	0.60	0.52	0.51	0.54
Grid thickness (mm)	1.2	2.1	3.6	6.2	10.7	18.6	6.2	6.2	30.0
Slat Material	Mo	W	W	W	W	W	W	W	W
Field of View (degrees)	1.0	1.0	1.0	1.0	1.0	1.0	4.4	7.5	2.8

of equal width, the transmission is time-modulated from zero to 50% and back to zero as the direction to the source changes. One cycle of this periodic transmission occurs for a change in source angle (in the plane orthogonal to the slits) of p/L where L is the separation between grids (1550 mm). The angular resolution is defined as $p/(2L)$. For off-axis sources, changing the angle between the source and collimator is achieved by rotating the spacecraft at ∼15 revolutions per minute.

2.2. Other Subsystems

The role of the detector and data system is to record the arrival time and energy of each photon detected, allowing the modulated count rate to be determined as a function of rotation angle.

The detectors, described by Smith *et al.* (2002), are high-purity germanium crystals, each electrically divided into front and rear segments. The ∼1-cm thick front segment is sensitive from 3 keV to ∼200 keV while the ∼7-cm thick rear segment extends the response to 17 MeV. Detector segmentation shields the rear segment from the intense flux of low-energy X-rays during moderate flares. Since the detectors themselves have no spatial resolution, they are optimized for high sensitivity and energy resolution. The detectors are mounted in a cryostat and are mechanically cooled to ∼75 K.

The electrical output pulse from each detected photon is amplified, shaped, digitized and passed to the Instrument Data Processing Unit (IDPU) (Curtis *et al.*, 2002). The IDPU stores information about each photon as a 32-bit event word that includes the detector ID, a 14-bit energy tag and the arrival time. This time is recorded with 1 microsecond resolution to enable all combinations of coincidence events between segments and detectors to be inferred during data analysis. A 4-Gbyte solid-state recorder, corresponding to almost 10^9 events, stores the data for periodic downloading. An average of 1.8 Gbytes per day is transmitted to the ground.

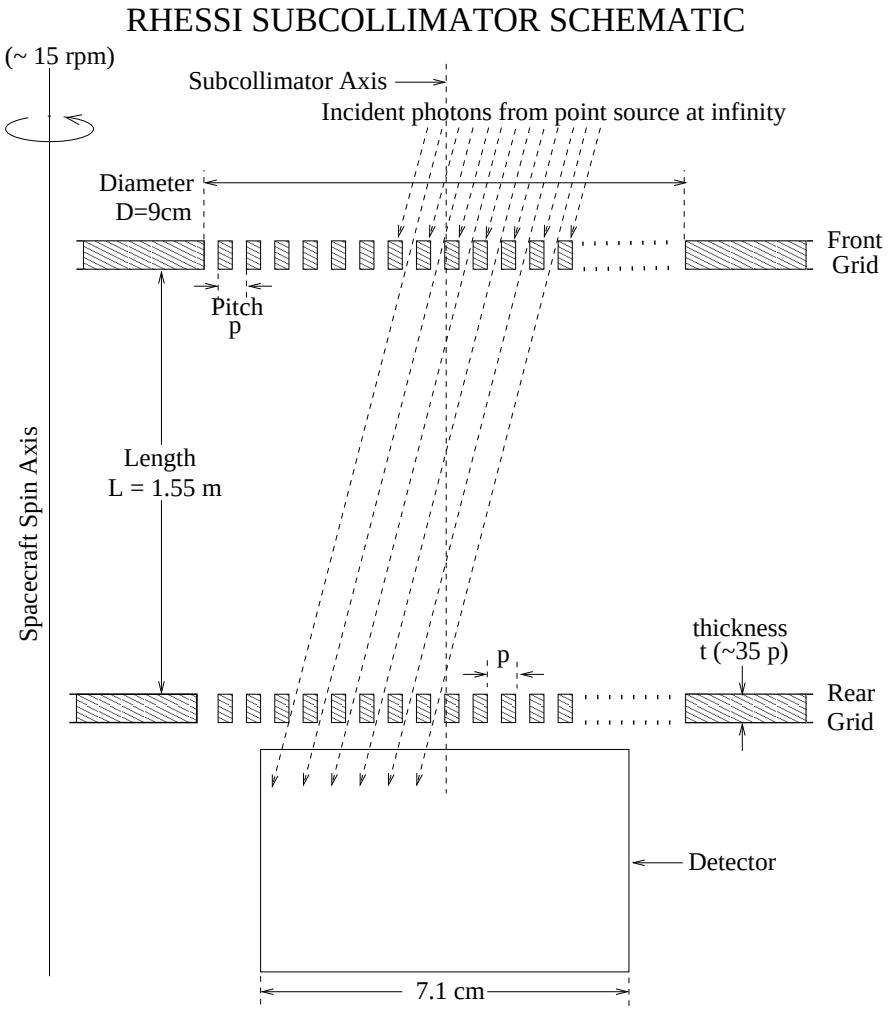

Figure 2. Schematic geometry of the *RHESSI* subcollimators, showing representative incident photons with respect to the collimator axis.

A high-bandwidth solar aspect system (SAS) (Zehnder *et al.*, 2002) permits substitution of accurate pointing knowledge for pointing stability, which need only be controlled to arcminutes. The SAS consists of 3 lenses in the front grid plane that focus solar images onto a set of 3 linear diode arrays in the rear grid plane. The solar limb is determined at 6 positions (2 per array) at rates up to 128 Hz (16 Hz typical), giving pitch and yaw to $\sim 0.4''$ rms.

Roll aspect is provided by one of two redundant star scanners. Imaging to date has used a Photo-Multiplier-Tube Roll Aspect System (PMTRAS) (Hurford and Curtis, 2002). This system views the star

field perpendicular to the Earth-Sun line and determines absolute roll to $\sim$ 1 arcminute by noting the times at which bright stars are detected as the spacecraft rotates. Data are also available from the other roll aspect system (RAS) (Zehnder *et al.*, 2002), which is based on a similar concept but uses a linear photodiode in place of the photomultiplier.

The data handling concept outlined above must accommodate potential count rates in excess of $10^6 s^{-1}$ detector^{-1} where the finite response time of the detector and data handling system become relevant (Smith *et al.*, 2002). This accommodation employs four techniques, the goals of which are to preserve the sensitivity to rare high-energy gamma-rays while maintaining the ability to image lower energy X-rays, whose incident flux can be $\sim$12 orders of magnitude higher.

The first technique is to apply corrections for the estimated dead time of the detector/electronics. Spare bits in the event words are used to encode this dead time with 512 microsecond time resolution. This is sufficient to follow the effects of modulation for all the grids.

Second, as the dead time becomes larger, on-board software commands either or both of two sets of nine aluminum attenuators (Smith *et al.*, 2002) to be mechanically inserted between the rear grids and the detectors. The attenuators reduce the flux of low-energy photons that reach the detectors while having no effect above $\sim$100 keV.

Third, when count rates become sufficiently high that they do not adequately characterize the modulation, an additional technique, capable of handling higher count rates, is automatically activated. In this 'fast rate mode', front detector counts are sorted into just 4 energy channels with time bins that are sufficiently short to preserve the modulation. This permits imaging at higher count rates than is possible by fully digitizing and time-tagging individual photons.

A fourth technique is used to deal with the finite size of the solid-state recorder. As the recorder becomes filled, a decimation scheme is automatically enabled to digitally discard a fixed fraction of front-segment events below an energy threshold. Both the fraction and the energy thresholds can be preset by ground commands. Discarding events in this way does not introduce any bias that would affect the modulation.

Two features of the detector response, both discussed by Smith *et al.* (2002), are particularly relevant in an imaging context. The first is that substantial data gaps (up to several hundred milliseconds) are observed. Since these gaps have a characteristic signature, the time and duration of their occurrence can be determined independently and are treated as periods of zero live time.

The second feature is pulse pileup (Datlowe, 1975) whereby two or more low-energy photons arrive 'simultaneously' and are indistinguishable from a single higher-energy photon. This has long been a complication for solar X-ray spectroscopy and at very high count rates it can also introduce artifacts in the imaging. The pileup counts are generated at a rate that goes roughly as the square of the detected low-energy count rates. Therefore they are also modulated but appear at higher energies. This can result in 'ghost' low-energy sources appearing in images nominally formed from high-energy photons.

3. Modulation Principles

3.1. The Modulation Profile

As described above, the *RHESSI* imaging hardware uses a set of rotating collimators to time-modulate the detected photon flux. To understand how this encodes imaging information, it is conceptually useful to adopt the perspective of a rotating coordinate system fixed on the collimator. From this perspective, in the typical case of a distant source that is slightly offset from the collimator axis (illustrated in Figure 2), the source moves in a circle about the rotation axis. The component of source motion parallel to the slits does not cause modulation. It is the simple harmonic motion perpendicular to the slits that modulates the count rates. (A characteristic of the resulting modulation is that while its frequency varies, it is locally periodic in time over a limited range of rotation angles.)

For a single source, the various panels in Figure 3 show how the resulting modulated count rates (modulation profiles) depend on the source intensity, location and size. The first panel, with which the others may be compared, shows the modulation profile of a single point source. The second panel assumes a source with the same location, but one half the intensity. Since the response of the the collimator/detector system is linear, changing the intensity of the source just decreases the amplitude of the modulation without changing its shape. The third panel shows the effect of moving the source in azimuth about the rotation axis. This shifts the modulation profile in time. Moving the source further off-axis increases the number of modulation cycles per rotation as shown in panel 4. Increasing the diameter of the source while keeping its total intensity the same (panel 5) reduces the amplitude of the modulation while leaving the time-averaged transmission unaffected. Further increases in source size (compared to the resolution of the collimator) reduce the modulation still further (panel 6).

In practice, of course, real sources may be more complex, and the sum of their multiple components yields a modulation profile such as illustrated in the last panel in Figure 3. Thus, the central data analysis task for *RHESSI* imaging is the inverse problem of deducing the source geometry, given a set of observed modulation profiles from the different subcollimators. Much of the remainder of this paper will be devoted to the different approaches taken to the solution of this problem.

We can set the stage for solving this inverse problem by digitizing the modulation profile into a series of time bins, and by describing the brightness distribution in the source plane as a pixelized image F_m, where F_m is the photon flux (photons cm^{-2} s^{-1}) from pixel m incident on *RHESSI's* front grids.

Neglecting background and for a specific energy interval, the following formal equation shows that the expected counts in the ith time bin is given by:

$$\mathcal{C}_i = A \sum_m P_{im} F_m \Delta t_i \tag{1}$$

In this notation, P_{im} is the probability that a photon originating in pixel m and incident on the front grid will be counted in the ith time bin during interval Δt by a detector with area, A. (Note that since m is the index of a two-dimensional map, P_{im} is really a numerical "cube".) Since P_{im} may be calculated from the grid properties and collimator aspect, the inverse problem can be summarized as follows: find the source map, F_m, given a measurement of count rates $\mathcal{C}_i$ in each time bin.

3.2. Describing the Grid Response

The solution of the inverse problem posed by Equation (1) requires a knowledge of P_{im}, the probability that a photon from map pixel m will be detected in the ith time bin. This requires calculation of the transmission probability of a grid pair as a function of energy and direction of incidence. In this section, we describe the approach taken to accomplish this.

To introduce this issue, we return briefly to the idealized case of thin, opaque grids with equal slit and slat widths, for which the rapid modulation takes on a basically triangular form between 0 and 50% as a function of offset angle. Since this time profile is periodic as a function of offset angle from the collimator axis, the transmission probability can be described in terms of the first few harmonics of its expansion as a Fourier cosine series containing only odd harmonics:

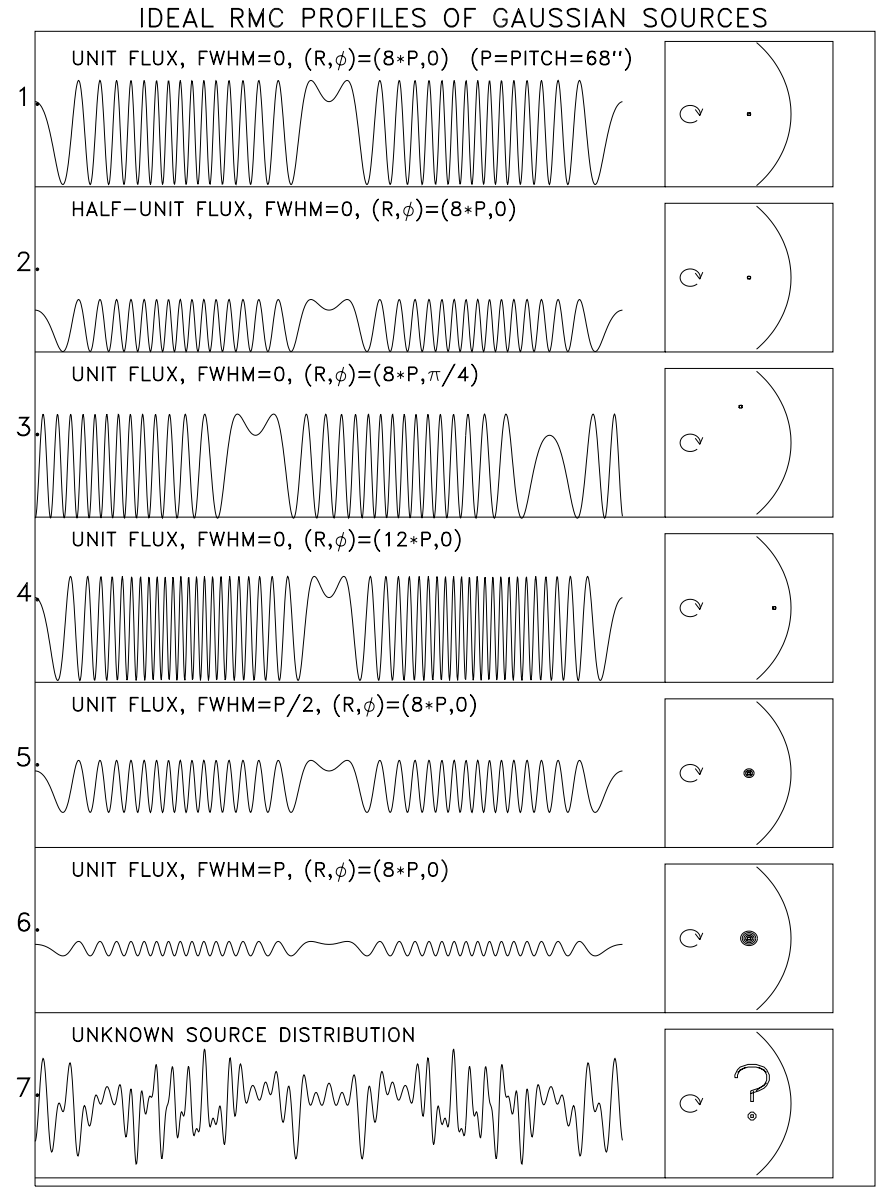

Figure 3. Modulation profiles plotted for one complete rotation for various configurations of an off-axis source, assuming ideal grids with equal slits and slats mounted on a collimator that is rotating uniformly about a fixed axis,. As discussed in the text, successive panels show the effect on the modulation profile of changing the source characteristics.

$$\wp_{triangle}(\Phi) = \frac{1}{4}\cdot(1+\frac{8}{\pi^2}cos(\Phi)+\frac{8}{9\pi^2}cos(3\Phi)+\frac{8}{25\pi^2}cos(5\Phi)+\cdots) \quad (2)$$

where $\Phi = 2\pi\theta L/p$. (p is the grid pitch; L is the distance between front and rear; θ is the angle of incidence in the plane orthogonal to the slits.) This is equivalent to the form used by Schnopper *et al.* (1970) for their observations of the Galactic center with a rocket-borne RMC.

There are several reasons why the triangular functions described by Equation (2) cannot be applied directly to *RHESSI*. As photon energies increase, the grids become transparent. The slits and slats are, in general, not equal. The peak transmissions are decreased by internal shadowing within each grid due to the large ratio of grid thickness to slit width (Table 1). The grids have imperfections, due to fabrication tolerances and to structural design features. Diffraction effects become relevant below ∼4 keV for subcollimator 1. Furthermore, these effects are not independent since, for example, some moderate energy photons, incapable of penetrating the grids directly, can penetrate the corner of a slat when they are incident from a few arcminutes off-axis.

In previous missions such as Yohkoh HXT, such effects were not as severe and so could be accommodated by modifying the triangular functional form and introducing more parameters (Sato *et al.*, 1999). However, for *RHESSI*, a different approach is necessary. All the factors identified above can be quantitatively described by generalizing Equation (2) to express the transmission of the grid pair in the form:

$$\wp(\Phi) = T\cdot(1+a_1\ cos[\Phi-\Psi_1]+a_2\ cos(2[\Phi-\Psi_2])+a_3\ cos(3[\Phi-\Psi_3])+\cdots) \quad (3)$$

where T is the average collimator transmission, a_i and Ψ_i are relative modulation amplitudes and collimator phases for the i^{th} harmonic. (In this terminology, harmonic 1 is the fundamental.) For ideal grids, these parameters would have fixed values, but for *RHESSI,* T and the other coefficients become slowly varying functions of angular offset and energy. Note that the expansion includes terms with even as well as odd harmonics. Use of the higher-order terms is in fact desirable since the 2^{nd} and 3^{rd} harmonics effectively increase the angular resolution of each grid by factors of 2 and 3 respectively, albeit with lower sensitivity. For *RHESSI* imaging to date, and for much of the remainder of this paper, we will assume that only the fundamental term is used. Because of the 'orthogonality' of the harmonics, this simplification introduces no 'bias' and only slightly degrades the signal-to-noise.

In summary then, the characteristics of real grids can be accommodated by treating the idealized triangles as sinusoids. As we shall see,

this approximation also enables considerable computational efficiency in the imaging algorithms.

3.3. The Imaging Geometry

Equation (3) shows how the grid transmission probability, $\wp(\Phi)$, can be expressed in terms of the angular offset θ orthogonal to the slits. In this section we establish how this is related to the P_{im} 'cube', in Equation (1), in the context of a mapping geometry for RHESSI imaging.

To begin the mapping process, the user chooses a map center, field of view and pixel size. Although the selected map center is arbitrary, it should be close to the centroid of the emission sources since the grid response parameters are calculated for the map center and their variation across the map is subsequently neglected. In practice, the map center can be found by coarse mapping or context observations, or by using previous knowledge of the flare position.

Figure 4 illustrates a typical map geometry with the map center defined in a heliographic coordinate system. The coordinates (x_m,y_m) of individual map pixels are defined in turn with respect to the map center.

An 'imaging coordinate system', fixed on the spacecraft, has its Z-axis defined by a vector between two fixed points on the front and rear grid trays. The projection of this vector onto the Sun is shown as the 'imaging axis' in Figure 4. In general, this axis is not coincident with the spacecraft spin axis, so the imaging axis will move with time. At any instant, however, its location relative to Sun center is provided by the aspect solution (Fivian and Zehnder, 2002). The orientations of the X and Y axes of the imaging coordinate system are fixed with respect to the spacecraft. As a result, their projection onto the Sun rotates (clockwise looking from the spacecraft), with the $Y_{imaging}$ axis making an angle α(t) with the heliographic Y axis.

A pair of grids is fixed in the imaging coordinate system with the slits oriented at a constant angle β, the 'grid-orientation', measured counter-clockwise with respect to the imaging Y axis. Lines of maximum response of the grid pair are indicated by the parallel dashed lines labeled 1-12 in Figure 4. These lines define the phases of the subcollimator. Note that a line of maximum response does not necessarily pass through the imaging axis and so for each subcollimator there is a phase offset (labeled Q). The quantity Q is the same as $-\Psi_1$ in Equation (3).

The map center lies at a radial distance r_0 from the imaging axis. Its phase with respect to that of the imaging axis depends on the

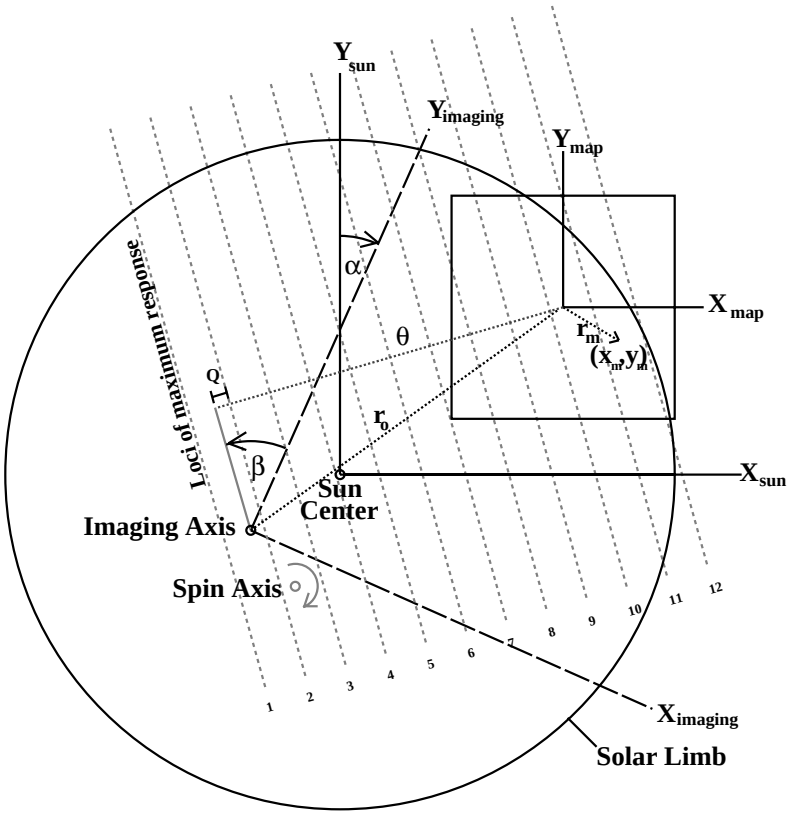

Figure 4. The imaging geometry. Solid lines and axes are fixed in heliocentric coordinates. Dashed lines and axes rotate clockwise with the spacecraft. Details are discussed in the text.

component of $\mathbf{r_0}$ orthogonal to the grids. This is shown by the dashed line labeled θ in Figure 4. For a source at map center, this is equivalent to the θ mentioned earlier as the angle of incidence perpendicular to the slits.

To simplify the calculation of the phase, we use a wavevector $\mathbf{K}$ with magnitude $K = 2\pi/p$ and orientation directed orthogonal to the slits (parallel to the line labelled, θ, in Figure 4). Then at time bin i the map-center phase with respect to the imaging axis is given by:

$$\Phi_{0i} = 2\pi\theta/p = \mathbf{K_i} \cdot \mathbf{r_{0i}} \tag{4}$$

Next we generalize this to sources anywhere in the map field of view. For a given subcollimator, the phase Φ (relative to the imaging axis) of a pixel m displaced from map center by $\mathbf{r}$, is given by

$$\Phi_{im} = \Phi_{0i} \ + \mathbf{K}_i \cdot \mathbf{r_m} \tag{5}$$

In principle, With this knowledge of Φ_{im} and grid parameters, T, a_i and Ψ_i appropriate to the energy and offset $\mathbf{r_0}$ we can calculate the response P_{im} as used in Equation (1). In practice, this calculation is aided by the introduction of an additional concept, the 'modulation pattern', discussed in the next section.

3.4. The Modulation Pattern

The two-dimensional *modulation pattern* characterizes the instantanteous response of the collimator. (It is not to be confused with the one-dimensional *modulation profile* which describes the response of a collimator vs time.) The modulation pattern can be thought of as a probability map on the Sun of the possible origin of a photon that was detected at a specific time. It is the (i=constant) plane in the 'cube' P_{im} whose calculation is described by Equation (5).

The modulation pattern is found, in one guise or another, in other domains of Fourier imaging. In radio astronomy, the modulation pattern is a projection of the complex *fringe pattern*. In the case of Yohkoh/HXT, there are 64 fixed modulation patterns, one for each of its subcollimators.

For *RHESSI* the modulation pattern for each subcollimator is fixed with respect to the rotating spacecraft. Relative to the grids, Equation (2) shows that by neglecting higher harmonics, the modulation pattern has a sinusoidal profile. The lines of maximum response shown in Figure 4 represent the peak contours of these profiles. Over the mapped area, we neglect any variation in the grid-dependent parameters in Equation (2).

Although the modulation pattern is fixed in the *rotating* frame of the spacecraft, a computational challenge arises because in the course of imaging, the 'cube' P_{im} must be evaluated over the *non-rotating* solar map which itself is drifting with respect to the imaging axis. This would require rotating and shifting the modulation pattern for each time bin before evaluating it at each map pixel. Computation and storage requirements render this impractical if done in a straightforward manner.

Two simplifications are used to deal with this. First, the mapping is done in polar coordinates, with an arbitrary origin well outside the mapping field of view. (The final map is converted back to Cartesian coordinates before display so that the use of polar coordinates is not seen by the user.)

Second, for each subcollimator the instrument response is calculated in terms of '*universal modulation patterns*'. One such pattern represents the modulation pattern (in polar coordinates) in a coordinate system fixed with respect to the imager. The second pattern is the same, except for a 90-degree phase shift. (This mimics the use of visibilities, described in the Appendix.) Consequently, the modulation pattern for any combination of rotation and shift can be calculated as the weighted sum of a subset of the elements of these pre-calculated *universal modulation patterns*. This approach saves an order of magnitude in computation time and memory, while remaining transparent to the user. Using these techniques the P_{im} 'cube' can be evaluated efficiently so that a map can be reconstructed by inverting the observed modulation profile as described by Equation (1). In the next section, we will outline the algorithms by which this is accomplished.

Before doing this, however, it is necessary to correct the observed modulation profile for the detector livetime. Specifically, in order to interpret the number of photons $\mathcal{C}_i$ incident on the detector, during the ith time bin, one must incorporate the live time τ_i (live time=observation time - dead time) (Smith *et al.*, 2002). When this is done, the expected number of counts, $\mathcal{C}_{im}$ in the ith time bin from a source with photon flux, F_m, at map pixel m is given by

$$\mathcal{C}_{im} = A \cdot F_m \cdot T_i \tau_i \{1 + \sum_n a_n^i cos[n(\Phi_{im} - \Psi_n^i)]\} \qquad (6)$$

where the subscript n refers to the n^{th} harmonic and the energy-dependent subcollimator transmission T_i, phase offsets, Ψ_n^i, and amplitudes a_n^i are evaluated at map center.

Exploiting the linearity of the detector and subcollimator response, the predicted modulation profile, $\mathcal{C}_i$ for any source, is just the sum over $\mathcal{C}_{im}$ for all nonzero pixels. As will be discussed in later sections, this predictive principle is used by several of the *RHESSI* reconstruction algorithms to assess the consistency between the reconstructed image and the observed modulation profiles.

4. Image Reconstruction

In this section we review the various image reconstruction algorithms that are used for *RHESSI* imaging. The general approach is to use a 'back projection' algorithm to generate an initial estimate of the image. This estimate represents a convolution of the source with the instrumental response and so has sidelobes. To improve the image quality (*viz* to reduce the sidelobes), one can then use a variety of techniques to be discussed below (Clean, MEM, MEMVIS, Pixons, Forward-Fitting). Each of these makes broad assumptions about the character of the source, and most proceed in a cycle of predicting the modulation profile for a test image, comparing the predicted and observed modulation profiles, modifying the test image and iterating until an 'acceptable' agreement is obtained.

4.1. Back Projection and Fourier Transforms

Back projection (Mertz *et al.*, 1986) is the most straightforward and basic method of image reconstruction. It is equivalent to a 2D inverse Fourier transform (Kilner and Nakano, 1989). A map constructed by this method is the analog of the radio astronomer's initial Fourier transform of the observed visibilities (the so-called 'dirty map'). Back projection is a linear process: maps for arbitrary time intervals may be added together, and maps for different pitches and harmonics may be summed, generally leading to improvement of the image. Further improvements to the image by Clean or MEM (for example) do not share this property of linearity.

As discussed above, at a given instant in time, the response of a detector is characterized by the modulation pattern of the corresponding subcollimator oriented according to the roll angle. Detected photons are most likely to have come from regions where the modulation pattern has its highest values.

Back projection builds up a map by summing over time bins. For each time bin the map is incremented by the product of the counts in that time bin and the corresponding modulation pattern. This process preferentially populates map pixels corresponding to the real source(s). Other pixels will be built up as well, but to a lesser extent, as determined by statistics and by the symmetries in the set of modulation patterns used. (It is easily shown, for example, that for a single subcollimator with a sinusoidal modulation pattern, rotationally averaging such a pattern results in a map which is proportional to a zero order Bessel Function $J_0(2\pi rL/p)$ whose first positive sidelobe is 30% of the peak.) For adequate statistics, many time bins, several detectors and

a mapped area that does not include the axis of rotation, the highest points in the back projection map will be at the location of the point source(s).

Mathematically, back projection can be described as follows. The modulation patterns P_{im} are computed and appropriately summed for all time bins i and map pixels m. Flat-fielding is necessary since the sensitivity is proportional to the variance of the modulation profile for each map point. This correction and normalization is implemented using a modified version of a recipe described by Durouchoux, *et al.* (1983). Subtract out the mean over all roll angles at each pixel: ($\widetilde{P}_{im} = P_{im} - < P_m >$). Then divide each value by its variance over all roll angles: ($\widehat{P}_{im} = \widetilde{P}_{im} / < \widetilde{P}_m^2 >$).

The intensity I_m of each pixel (m) in the back-projection map is defined by the following linear combination of the count rates $\mathcal{C}_i$:

$$I_m = \frac{1}{A} \sum_{i=1}^{N} [\mathcal{C}_i / \Delta t] \cdot \widehat{P}_{im} \tag{7}$$

where A is the effective area (cm^2) of the detector and Δt is the time-bin duration (s). The normalization and the division by $A\Delta t$ ensures that the expectation value at the peak of the dirty map equals the strength of a dominant source. The map then has units of counts $cm^{-2}s^{-1}$. In practice, a slightly more complex formulation is used to distinguish between the variance component due to modulation and the variance component due to the twice-per-rotation changes in transmission grids caused by internal shadowing in individual grids.

Figure 5 shows an example of a back-projection image for a compact flare source whose spatial size is smaller than the subcollimator's angular resolution. The full-disk image, which uses the three coarsest subcollimators, shows the characteristic ringed patterns caused by incomplete sampling of the Fourier plane. Noteworthy is the "mirror" source seen in the lower left quadrant of the full-disk map. This is a consequence of not having both "sine" and "cosine" subcollimators, but is not a problem in practice since the mapped area usually includes only the real source. In this case, consistency among maps made by individual subcollimators shows that the true source is on the limb in the upper right. Exactly halfway between the true and mirror sources is the spin axis, where no modulation occurs. The small-field back-projection map, made with subcollimators 3-8, shows the flare surrounded by rings whose amplitude is smaller than in the full-disk map due to the use of a larger number of subcollimators.

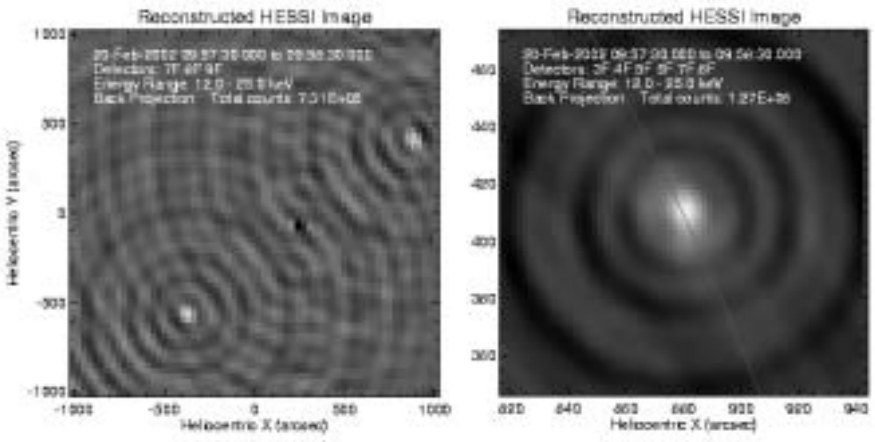

Figure 5. RHESSI full-Sun and small-field back-projection images for a compact flare that occurred on 23-Feb 2002. The pixel sizes are $32''$ and $2''$ respectively. Insets indicate the subcollimators used and other details.

All of the practical image reconstruction algorithms for improving a back-projection ('dirty') map are nonlinear. In the following section, we describe some of the options currently implemented.

4.2. Clean

Clean is an iterative algorithm, originally developed for radio astronomy, which is based on the assumption that the image can be well represented by a superposition of point sources. Nevertheless, it is often satisfactory for extended sources as well. Adapted to *RHESSI*, the basic Clean method, developed by Högbom (1974), postulates that the observes 'dirty' map is a convolution of a set of point sources with the instrument Point Spread Function (PSF) (viz, the imager's response to a delta function source). That is,

$$D = \mathcal{P} \otimes I_{source} \tag{8}$$

where $\mathcal{P}$ is the PSF for one or many subcollimators and/or harmonics, I_{source} is the source distribution, D is the back projection ('dirty') map and $\otimes$ denotes a convolution.

The algorithm proceeds as follows. An image called the 'residual map' is initialized with the back-projection map, to a value I_0. Then the position (x_j,y_j) of the pixel with the largest flux F_j in the residual map is saved in a 'Clean component' table. The PSF $\mathcal{P}$ at (x_j,y_j), normalized to μF_j (where μ ($\leq$1) is the so-called 'loop gain'), is subtracted from the current residual map, I_n to yield a new residual map I_{n+1}. This

process is continued iteratively until a specified number of iterations is reached, until the residual map contains a negative peak which exceeds the largest positive peak, or until the observed modulation profile agrees well with that predicted from the Clean components as indicated by a chi-squared test.

Since the final residual map, (I_{final}) presumably consists mainly of noise, the information content of the Clean map is contained in the table of the amplitudes and locations of the Clean components. For the purposes of display, these Clean components are convolved with a Clean PSF (or 'Clean Beam'), $\mathcal{P}_{Clean}$, which is a simply a gaussian whose FWHM reflects the effective resolution of the subcollimators used for the dirty map. The final Clean map

$$I_{clean} = \sum_j \mathcal{P}(x_j, y_j)\mu F_j + I_{final} \tag{9}$$

represents the sum of the Clean components, convolved with the Clean PSF, plus the final residual map. With Clean (unlike the other algorithms) the latter is added to provide a visual estimate of noise in the final map.

A final detail is that, for computational efficiency, the Clean processing is done in polar coordinates, although results are transformed back to rectangular coordinates for display.

Figure 6 shows examples of back projection, Clean, and other techniques discussed below.

4.3. Maximum Entropy Methods

The goal of Maximum Entropy Methods is to find the map that is both consistent with the data and that contains the least information about the source. While not explicitly required, this condition generally makes MEM maps appear quite 'smooth' compared to other techniques.

MEM has a rich history and has been used as the main image reconstruction algorithm for Yohkoh/HXT. Although the details of the 'MEM-Sato' implementation are somewhat different for *RHESSI,* the basic theory is still relevant (Sato, 1998; Sato, *et al.*, 1999).

To implement MEM-Sato for *RHESSI*, the list of time-tagged photons for each subcollimator and energy band are converted to a set of counts in time bins, each of which corresponds to a particular roll angle. Traditionally, consistency of a map with the data is measured using a χ^2 measure on the counts:

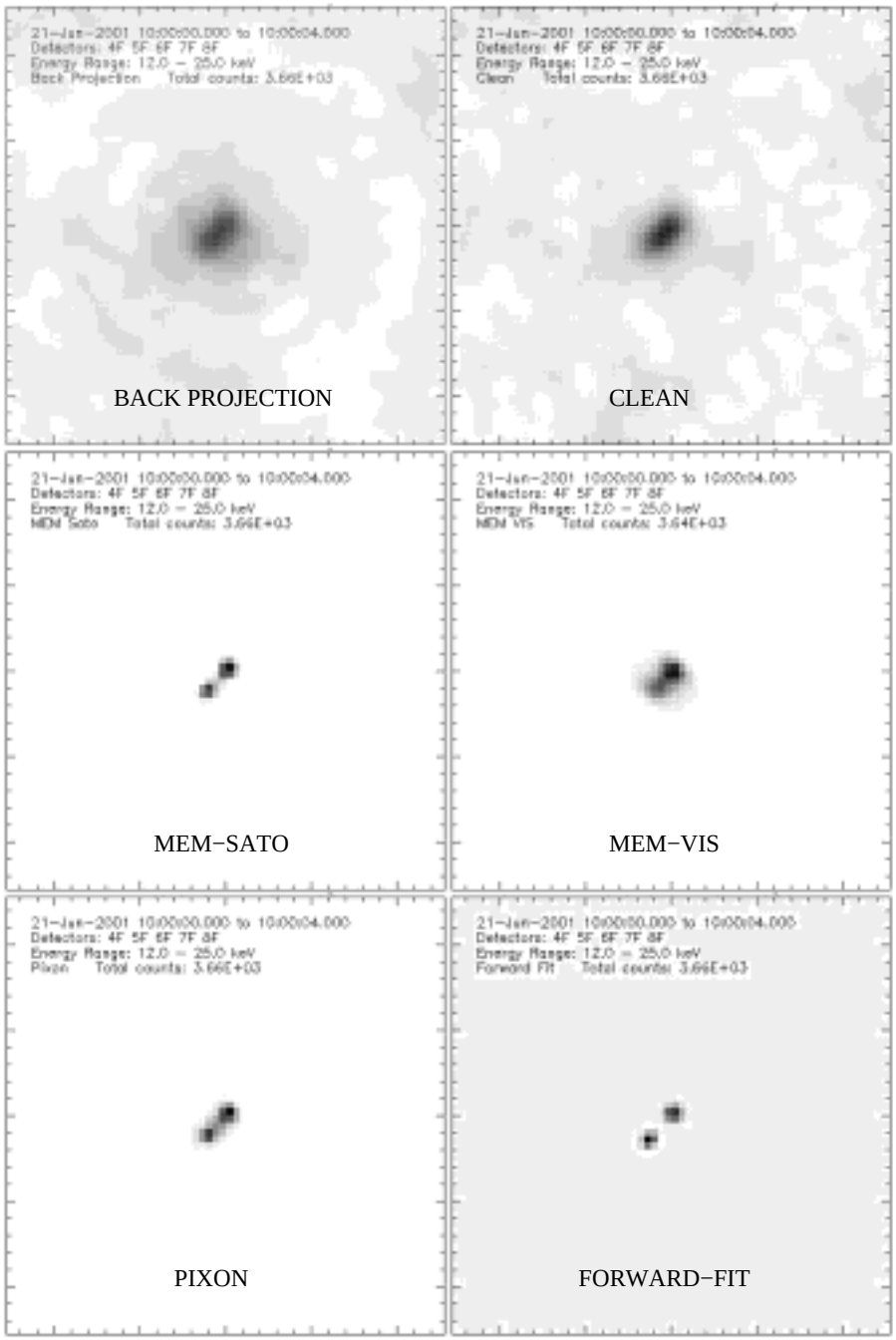

Figure 6. Example back-projection, Clean, MEM-Sato, MEM-vis, Pixons, and pixelized Forward-Fit maps of a simulated double source. Two identical point sources were located 17″ apart. The pixels are 4″ and the FOV is 256×256″. 5 subcollimators with resolutions ranging from 12″ to 106″ were used.

$$\chi^2 = \sum_i \frac{(\mathcal{C}_i - \mathcal{E}_i)^2}{\sigma_i^2} \tag{10}$$

where $\mathcal{C}_i$ is the observed count for time bin i; $\mathcal{E}_i$ is the 'expected' count from the reconstructed image; and σ_i is the estimated uncertainty of count $\mathcal{C}_i$. If only photon counting noise is important, then $\sigma_i^2 = \mathcal{E}_i$, but in practice systematic errors and the background may also be significant and so should be included in σ_i. Since it is quite common to have fewer than 10 counts per time bin (in which case χ^2 is inaccurate), the MEM-Sato algorithm uses the more rigorous C-statistic (Cash, 1979) instead. (For simplicity, however, we will continue to use the term, χ^2 in this paper.)

The condition of minimizing the information about the source is quantified using an entropy measure. In one view, the entropy is a quantity that, when maximized, produces a positive image with a compressed range in pixel values (Cornwell, 1984), but according to Gull and Skilling (1984) and Sivia (1996) the only function which guarantees that no unwanted correlation be imposed is:

$$\mathcal{H} = -\sum_m F_m \log F_m \tag{11}$$

where F_m is the flux in pixel m. The balance between maximizing entropy and consistency with the data is implemented by maximizing $\mathcal{Q} = \mathcal{H} - \frac{\lambda}{2}\chi^2$ for the smallest possible λ. In practice λ is set to a small value initially and an image is sought iteratively that has $\chi^2 = 1$ (*viz*, consistent with observations). If such an image cannot be found, the entropy constraint is eased by increasing λ. Additional constraints (*e.g.* total flux) can be added to $\mathcal{Q}$ if desired. Examples of MEM-Sato imaging can be found in Sato (2002).

Another approach to the Maximum Entropy Method involves the conversion of the list of time-tagged photons to visibilities. As explained in the Appendix, this effectively converts the observed modulation profile to an equivalent representation of amplitudes and phases as a function of grid orientation. Another *RHESSI* image reconstruction algorithm, MEMVIS, then applies MEM to the visibilities instead of to the binned counts. This algorithm will be discussed in detail in a forthcoming paper by Conway, Schmahl and Hurford.

The main advantages of MEMVIS are its efficiency (lower memory requirements, use of fast Fourier transforms) and the ease by which the visibilities can be integrated over time by *literally* just adding them together. Simulations have shown that MEMVIS appears to be quite robust at low count rates.

Figure 6 includes examples of MEMVIS and MEM-SATO maps.

4.4. Forward-Fitting

The Forward-Fitting method is based on the assumption that the spatial map can be well represented by a small number of elemental source structures, each of which can be characterized by just a few parameters. In a solar hard X-ray context, such structures might be circular, elliptical, or curved elliptical Gaussians (which resemble a loop). Such Gaussian sources can be represented by 4, 6 or 7 parameters respectively. Examples of fits to hard X-ray sources observed by Yohkoh/HXT may be seen in Aschwanden *et al.*, 1999.

In the Forward-Fitting algorithm implemented for *RHESSI* (Aschwanden *et al.*, 2002), "pixelized" maps of multiple Gaussian components are created and used to calculate a model modulation profile which is then compared to the the observed modulation profile. The map iteratively evolves into a best-fit image which yields well-quantified parameters. Alternative forms of Forward-Fitting without discrete pixelization have also been used for RHESSI source parametrization (Schmahl and Hurford, 2002).

4.5. The Pixon Method

The Pixon method is another technique which removes the sidelobe pattern of a telescope while mitigating the problems of correlated residuals and spurious sources which are commonly seen in Fourier deconvolution and maximum entropy approaches.

The goal of the Pixon method is to construct the simplest model for the image that is consistent with the data (i.e., having an acceptable χ^2 fit). Being the simplest model, the derived image would be artifact free with no spurious sources. The model is necessarily the most tightly constrained by the data, and consequently has the most accurately determined parameters (Puetter, 1995; Metcalf *et al.*, 1996; Alexander and Metcalf, 1997).

MEM imposes a global condition that minimizes the difference between the image and a grey map in a manner that is consistent with the data. The Pixon method is related to MEM, but applies a local constraint such that structure is allowed only where required by the data. (From an information science point of view, one selects a model from the family of multi-resolution basis functions (Pixons) that both has the minimum information content and statistically fits the data.)

Since the model has minimum complexity, spurious sources are unlikely to arise. Each parameter is determined using a larger fraction of

the data and so is determined more accurately. This usually results in superior photometric and positional accuracy and, since the minimum number of parameters are used, the data cannot be over fitted. The Pixon method, however, pays a price for its photometry: the method is one to two orders of magnitude slower than the other reconstruction methods. Therefore, as with Yohkoh/HXT, it will probably be used only after the faster reconstruction techniques have been used to optimize the time and energy binning. Pixons can then be used to check the strength, shape or presence of weak sources as required.

5. Imaging Performance

5.1. Imaging Strengths and Limitations

Although it is too early in the mission to provide a definitive summary on imaging performance, the general properties of *RHESSI* imaging can be broadly outlined. This is important since RMC imaging has very distinctive strengths and weaknesses compared to conventional imaging instruments and these properties are directly relevant to the kind of science that can be done with *RHESSI* imaging.

RHESSI was not designed to provide images with the kind of morphological richness and detail that we have come to appreciate from TRACE, Yohkoh/SXT, SOHO/EIT and other direct-imaging instruments. Instead, *RHESSI* imaging determines the flux, location, size and shape of the dominant source components. Its measure of image quality is 'dynamic range', defined as the ratio of the surface brightness of the strongest source to the weakest credible source in the field of view. The design goal (and current expectation) is that in favorable circumstances a dynamic range of ∼100:1 can be achieved.

There are four broad factors that limit the quality of *RHESSI* imaging. The first is the limited number of spatial frequencies that are measured. For typical maps, sampling the Fourier components measured by the 9 rotating subcollimators provides $\sim 10^3$ independent measurements. Although this represents a substantial gain over Yohkoh/HXT, it still represents a fundamental limit to the complexity of the images that can be generated. This limitation becomes more severe if imaging is done on timescales of less than one half of the rotation period.

The second factor is photon statistics, which can be an important constraint. In very favorable circumstances, a point source can be detected and located with as few as $\sim 10^2$ counts. Usually, however, $\sim 10^3$ are required and for more complex images it is preferable to have 10^4 or 10^5 counts. (For comparison, a large flare returns over 10^8 counts.)

Third, the imaging algorithms ultimately rely upon comparisons of observed count rates to 'predictions' based on convolving test maps with the instrument response. Therefore, in circumstances with good statistics and simple sources, imperfect knowledge of the grid response, detector response and/or aspect solution can provide a limitation. At present the grid response is believed to be known at the ∼2% level. Good progress continues to be made in understanding the detector response (Smith *et al.*, 2002), which can be relevant at high count rates.

The fourth factor is the validity of assumptions that are implicit in the imaging algorithms. Such assumptions include the short duration of time bins compared to the modulation period, the uniformity of instrument response over the selected energy range, the uniformity of instrument response over the imaging field of view, the absence of temporal structure in the flux (on timescales that are commensurate with the modulation), the neglect of background in current implementation of some algorithms, and the neglect of off-diagonal elements in the spectral response matrix (Smith *et al.*, 2002) and the accuracy of corrections for live time and pulse pileup.

In general, *RHESSI* imaging has proven to be remarkably robust, a feature which permitted the generation of viable images early in the mission and in situations where the foregoing assumptions were not strictly valid.

The strengths of this imaging technique include the ability to accurately and absolutely (∼1 arcsecond) locate the source components on the Sun. This supports both reliable comparisons of images as a function of time and energy and accurate co-location with images in other wavelength regimes.

Photometric reliability of *RHESSI* images depends on the circumstances and is expected to improve. At present, it is typically at the ∼10% level, which is sufficient to support some feature-based imaging spectroscopy. Source sizes can also be determined (*e.g.* Schmahl and Hurford, 2002), although at present this requires careful interpretation of the images.

Finally, one of the underlying strengths of *RHESSI* imaging, derived from the photon-based nature of the data, is the analyst's ability to select the time resolution and range, energy resolution and range, imaging field of view, resolution and reconstruction technique (Schwartz *et al.*, 2002). These choices can be made and iterated during data analysis on the ground rather than in the mission design or operations phase. This enables these tradeoffs to be made in a manner that takes into account the characteristics of the flare and the specific science objectives of the

analyst. In practice this is perhaps one of the most valuable and novel features of *RHESSI* imaging.

5.2. Self-Calibration

As discussed above, one of the potential limitations to image quality is the knowledge of the grid response. However, one of the features of *RHESSI* imaging is the ability to self-calibrate this response. While a discussion of this feature is beyond the scope of this paper, it is perhaps worth mentioning the progress made to date. In particular, the relative 'phases' of the grids are vital parameters. For each grid this represents the average position of the center of the slats with respect to the imaging coordinate system defined by the solar aspect system. The current determination of these phases is based on maximizing the response of the system to unresolved sources. The accuracy of these determinations appears to be $\sim 10^{-2}$ of the grid pitch. A more sensitive technique, based on the stability of imaging using even and odd half-rotations, will be used to improve this further.

Other grid response parameters, such as the average transmission, can be verified by comparison of spatially integrated spectra obtained from each of the nine detectors. Interpretation of these ratios as a function of energy and offset angle is a sensitive diagnostic that can be used to fine-tune our knowledge of the grid parameters.

5.3. Expected Evolution of Imaging

During the course of the *RHESSI* mission, lessons are being learned about unanticipated features of the hardware and software. An example of such a lesson is the existence of data gaps (Smith *et al.*, 2002). As in other missions, the imaging software is expected to improve as bugs are eradicated and better algorithms are developed. In particular, we anticipate introducing an alternate approach to combining counts from multiple time bins that will greatly facilitate integration over long time periods. Also, the thus far neglected 2^{nd} and 3^{rd} harmonics of the grid response will be taken into account. For strong flares, this has the potential to improve the angular resolution of the grids by factors of 2 and 3, respectively. An important feature of these improvements is that in all cases they will be applicable retroactively to data acquired from the start of the mission.

5.4. Conclusion

In choosing an imaging concept for *RHESSI*, the selection of rotating modulation collimators was driven by the goals of high angular resolution, high sensitivity, good image quality and a 4-decade range of energies, all to be implemented within the practical constraints of a SMEX-class mission. As an additional feature, the photon-tagged data stream has afforded an unprecedented level of analysis flexibility to the user. Initial indications are that the *RHESSI* imaging technique has succeeded in providing imaging spectroscopy to meet these goals.

Nevertheless, the imaging concept does carry a cost, one imposed by its unfamiliarity and by the need for users to reconstruct images before they can proceed toward their real goal of addressing science issues. Effective image reconstruction relies upon an effective integration of of the hardware design, the analysis software and the user. This paper has attempted to describe the imaging concept that unifies these three elements.

6. Acknowledgments

We would like to thank the PSI team led by Alex Zehnder for the care, technical expertise and professionalism they demonstrated in fabricating the imager. We are also grateful to Dave Clark at GSFC for numerous insights and contributions to the imager alignment and calibration. Support for EJS came from NASA grant NAG 5-10180 to the University of Maryland. This work is supported by NASA grant NAS5-98033-05/03.

7. Appendix: Visibilities

The concept of visibilities is borrowed from radio astronomy. In the context of *RHESSI*, 'counts' and 'visibilities' can be regarded as two time series that present the same information: the response of *RHESSI* to a spatial flux distribution. The visibilities are complex and effectively contain two count profiles. The real (cosine) part can be regarded as (mean-subtracted) counts from a cosine subcollimator, and the imaginary (sine) part corresponds to an identical subcollimator shifted by one quarter pitch perpendicular to the slats (a shift of 90° in phase) i.e. a sine subcollimator. (In Equations (2) and (3), Φ would be replaced by $\Phi + \pi/2$.) Roughly speaking, the two parts of each visibility together contain the phase information provided by the aspect system and the

amplitude provided by the detectors. The visibilities include the corrections for pointing excursions, transmission variations, and detector sensitivity effects, and so the inverse Fourier transform need only be applied to obtain a 'dirty' map of the source, with most instrumental artifacts removed.

It is worth mentioning that in early versions of RMC design, there were both sine and cosine subcollimators (*e.g.*, Mertz *et al.* 1986, Murphy, 1990), which would give the visibilities more directly. But our experience has shown this to be unnecessary in hardware, since with sufficient sampling of the modulation profile, relative amplitudes of the sine and cosine components can be determined from the modulation profile itself.

Clearly *RHESSI* imaging has much in common with radio astronomy interferometry and could benefit from the enormous efforts invested in that subject. Also, we have found that the use of visibilities with *RHESSI* has several intrinsic and unexpected advantages. Here we outline how a visibility can be related to the count modulation profiles for a point source. A more complete account of visibilities and Fourier space in the context of *RHESSI* will be given in a forthcoming paper by Conway, Schmahl and Hurford.

A visibility is the value of the 2D Fourier transform of a spatial flux distribution at a point in Fourier space. It can either be expressed in terms of a discrete pixel image, as for the counts in Equation (1) with $P_{jm} = \exp(i\Phi_{jm})$, j and m labeling time bin and pixel respectively, or for a continuous distribution $F(x, y)$ at time j:

$$\mathcal{V}(u, v) = \int\int F(x, y) e^{i\Phi(x,y;u,v)} dx dy \tag{12}$$

where (u, v) are the coordinates in Fourier space determined by the subcollimator's pitch p and the current angle α_j of the grid slats. In fact the polar coordinates in Fourier space are just $(1/p, \alpha)$ where $u = (\cos\alpha)/p$ and $v = (\sin\alpha)/p$. The pitch determines the angular spatial frequency of a subcollimator $K = 2\pi/p$.

The visibility of a point source of flux F_0 at coordinate (x, y) or (r, θ) is therefore

$$\mathcal{V}(u, v) = F_0 e^{i\Phi} \quad \text{where} \quad \Phi = 2\pi(ux + vy) = Kr\cos(\theta - \alpha) \tag{13}$$

For the same source, a *RHESSI* count modulation profile can be expressed as follows by combining Equations (2) and (3):

$$\mathcal{C} = F_0 T\tau\,(1 + a_1\cos(\Phi - \Psi_1) + \text{harmonics}) \tag{14}$$

Comparison of Equations (13) and (14) reveals that the real part of the visibility, $F_0 \cos \Phi$, is similar to the second term in (14), aside from a known amplitude factor of $T\tau a_1$ and a known phase offset of Ψ_1. From this it is clear that a RHESSI subcollimator of a particular pitch at a particular roll angle is providing a measure closely related to the Fourier transform, i.e. visibility $\mathcal{V}(u, v)$, at a particular point in Fourier space. Over the course of a rotation, the (u,v) points for a particular subcollimator sweep out a complete circle in Fourier space. Subcollimators of smaller pitch sweep out larger circles on the Fourier plane. Note that while coverage along the circles can be excellent with *RHESSI* (given enough counts to fill the timebins), the Fourier transform in regions between the circles remains unknown.

The details of how counts are converted to visibilities are beyond the scope of this paper, though we will outline the process here. Firstly, we assume, as all imaging algorithms do, that the X-ray flux is restricted to a localized area of the Sun. This allows us to calculate the phase at map center for each time bin. Secondly, the mean subtracted counts are fitted with cosine and sine time series. This is done so that only the first harmonic is fitted in the time series, which is all we need for the visibilities. The coefficients from these fits can then be used to yield the real and imaginary parts of visibilities. However these visibilities are based on an origin on the spin axis, which moves with respect to the Sun. It is then necessary to apply a correction, which simply involves multiplying each visibility by a complex number, to bring the visibilities to some fixed center (either that of the Sun's disk or the map).

Figure 7 illustrates the close correspondence between count rate profiles and visibility profiles. The first panel shows a simulated modulation profile for two point sources about $1\frac{1}{2}$ angular pitches apart. This shows the beating of the sources in the form of slow modulation of the amplitude. The second panel shows the visibilities computed for the same sources. The cosine component (real part) of the visibility precisely mimics the amplitude and phase of the count modulation. The dotted curve shows the sine component (imaginary part), 90° out of phase with the cosine component. The amplitude and phase are shown in the third panel. The amplitude, which equals the root quadratic sum of the sine and cosine components, is the envelope of the modulated curves. The phase wraps from $-180°$ to 180° and back again as the lines of constant phase (see Figure 4) move across the source.

The units used in visibilities warrant some further discussion. According to Equations (13) and (14), the minima-to-maxima variation of the visibilities is several times larger than that of the counts. (Compare the ordinates of the first two panels of Figure 7.) In fact, when the

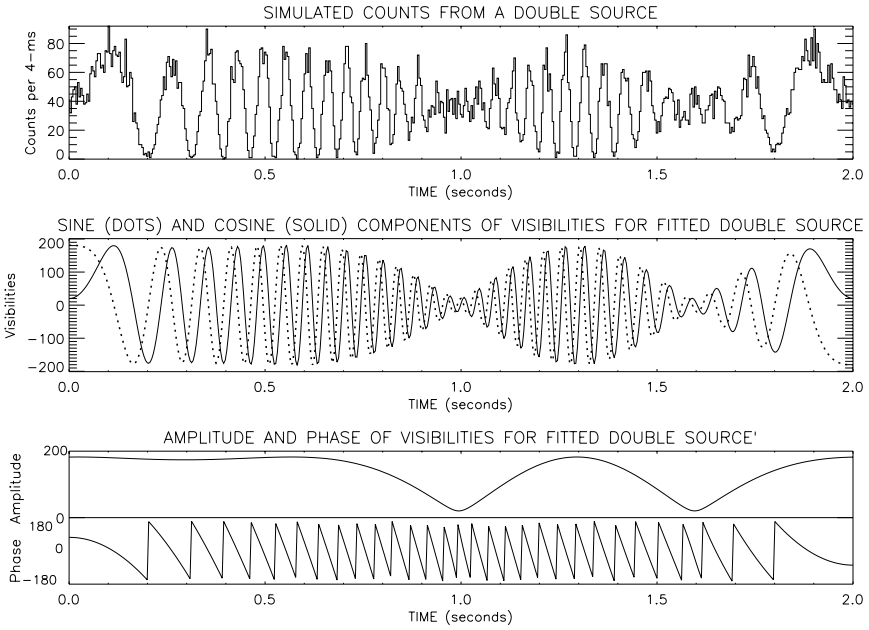

Figure 7. First panel: simulated count rate profiles for a double source of 10,000 counts s^{-1} $subcoll^{-1}$. Note the beating of the sources, which are about 1.5 angular pitches apart. Second panel: The solid curve is the real part (cosine component) of the visibility, and the dotted curve is the imaginary part (sine component). The cosine component reproduces the count rate profile precisely in amplitude and phase. Third panel: Amplitude and phase of the visibilities.

subcollimator pattern is ideal and perfectly triangular, ($a_1 T = 2/\pi^2$), the minima-to-maxima variation of $Re[\mathcal{V}_j]$ is $\pi^2/2 = 4.9$ times that of the count profile. Note also that our definition of visibility is such that the amplitude of the visibility for a point source is equal to its flux F_0. The amplitude for an extended source of the same flux will be less that F_0 if the source size exceeds the angular resolution. This means that the individual visibilities do not necessarily contain information on the total flux of the source, F_0 — an important fact to remember in creating images using visibilities. In practice, this is not a problem because F_0 can be estimated from the counts during the visibility construction process.

In working with *RHESSI* data visibilities offer a convenient intermediate between the observed counts and images that have been corrected for all of the spin-axis excursions, slit-shadowing, transmission and dead time effects. Since visibilities are essentially counts from an ideal subcollimator, it is easy to perform a graphical analysis on the visibilities, as illustrated in Figure 3. This kind of analysis can yield estimates of

the position and size of a source that are free from the assumptions (usually smoothness) that must be made to construct images.

Potential disadvantages of using visibilities are the introduction of a systematic error and a correlation of noise on visibilities in neighboring time bins. There is also the problem that since visibilities are constructed from two or more adjacent time bins successive visibilities are not truly independent quantities. However, from our experience with many simulated sources we can summarize the advantages of using visibilities as follows:

1. The aspect correction can easily be applied while constructing visibilities from the observed counts.

2. Due to 1, visibility modulation patterns do not need to be corrected for the aspect solution for each time bin.

3. Due to 2, operations involving modulation patterns can be performed with a convolution based on Fast Fourier Transform methods rather than a matrix multiplication. This allows a speed up of order M^2 as compared to $M \log M$, where M is the number of time bins.

4. Due to 2, integration of visibility values over several rotations simply involves adding together visibility series from those rotations.

5. In constructing visibilities from observed counts, there is effectively a smoothing, which relaxes problems arising from the presence of zero counts.

6. Visibilities provide a platform for using widely available imaging programs from radio astronomy. Although this capability is not presently available in the *RHESSI* software, only a module that writes visibility FITS files is needed to export *RHESSI* data to *AIPS* or other imaging systems.

References

Aschwanden, M., Schmahl, E. J. and the RHESSI Team: 2002, *Solar Phys.*, this volume.

Aschwanden, M., Fletcher, Sakao, Kosugi, T. and Hudson, H.S.: 1999, *Astrophys. J.* 517, 977.

Alexander, D. and Metcalf, T. R.: 1997, *Astrophys. J.* 489, 422.

Cash, W.: 1979, *Astrophys. J.* 228, 939.

Cornwell, T. J.: *Indirect Imaging, Proc. IAU/URSI Symp.*, ed. J.A. Roberts, Cambridge Univ. Press, 291, 1984.
Crannell , C. J., Hurford, G. J., Orwig, L. E. and Prince, T. A.: 1986, SPIE 571, 142.
Crannell,C.J.: American Institute of Aeronautics and Astronautics: Washington DC, AIAA-94-0299, 1994.
Curtis, D.W. et al.: 2002, *Solar Phys.*, this volume.
Datlowe, D. W.: 1975, *Space Sci. Instrumentation*, 1, 389.
Durouchoux, P., Hudson, H., Hurford, G., Hurley, K., Matteson, J., and Orsal, E.: 1983, *Astron. Astrophys.* 120, 150.
Enome, S.: 1982, *Adv. Space Res.* 2/11, 201.
Fivian, M. and Zehnder, A.: 2002, Solar Phys. this volume.
Gull, S. F. and Skilling, J.: 1984, IEE. Proc. 131(F), 646.
Högbom, J. A., 1974: *Astron. Astrophys.* 15, 417.
Hurford, G. J. and Curtis, D.: 2002, *Solar Phys.*, this volume.
Kilner, J.R. and Nakano, G.H.: 1989, S.P.I.E. 1159, "EUV, X-ray, and Gamma-Ray Instrumentation for Astronomy and Atomic Physics", 27.
Kosugi, T., et al.: 1991, *Solar Phys.* 136, 17.
Lin, R. *et al.*, 2002: *Solar Phys.*, this volume.
Makishima, K., et al.:1977, *New Instrumentation for Space Astronomy*, (K.A. van der Hucht and G.Vaiana eds.), New York, Pergamon Press.
Mertz, L. N., 1967: Proc. Symp. on Modern Optics, v. 17 of the *Microwave Research Institute Symposia Series* (Polytechnic Institute of Brooklyn), New York.
Mertz, L. N., Nakano, G. H., and Kilner, J. R.: 1986, *J. Opt. Soc. Am.* 3, 2167.
Metcalf, T. R., Hudson, H. S., Kosugi, T., Puetter, R. C. and Piña, R., K.: 1996, *Astrophys. J.*, 466, 585.
Murphy, M. J.: 1990, *Nucl. Instr. and Methods in Physics Research*, A290, 551-558.
Ohki, K., et al.: 1982, Proc. Hinotori Symp. on Solar Flares, ISAS, Tokyo, Japan, p. 102.
Prince, T. A., Hurford, G. J., Hudson, H. S., and Crannell, C. J.: 1988, *Solar Phys.* 118, 269.
Puetter, R. C., 1995: *Int. J. Image Systems Technol.* 6, 314.
Sato, Jun: 1998, PhD Thesis, NAO.
Sato, J.: 2002, Solar Phys., this volume.
Sato, J., Kosugi, T., Makishima, K.: 1999, PASJ, 51, 127.
Schmahl, E. J. and Hurford, G. J.: 2002, *Solar Phys.*, this volume.
Schwartz, R. *et al.*: 2002, *Solar Phys.*, this volume.
Sivia, D.S.: 1996, *Data Analysis, a Bayesian Tutorial*, Clarendon Press, Oxford.
Schnopper, H. W., Thompson, R. I., and Watt, S.: 1968, *Space Sci. Rev.* 8, 534.
Schnopper, H. W. et al.: 1970, *Astrophys. J.* 161L, 161.
Smith, D. *et al.*., 2002, *Solar Phys.*, this volume.
Van Beek, H. F., Hoyng, P., Lafleur, B., and Simnett, G. M.: 1980, *Solar Phys.* 65, 39.
Zehnder, A. *et al.*: 2002., SPIE Proceedings 4853, in press.